Phys. Med. Biol. **45** (2000) 1781–1805. Printed in the UK PII: S0031-9155(00)09776-1

150–250 MeV electron beams in radiation therapy

C DesRosiers†, V Moskvin†, A F Bielajew‡ and L Papież†

† Department of Radiation Oncology, Indiana University School of Medicine, 535 Barnhill Drive, Indianapolis, IN 46202, USA

‡ Nuclear Engineering and Radiological Sciences, University of Michigan, 2355 Bonisteel Blvd. Ann Arbor, MI 48109, USA

Received 22 November 1999, in final form 11 February 2000

Abstract. High-energy electron beams in the range 150–250 MeV are studied to evaluate the feasibility for radiotherapy. Monte Carlo simulation results from the PENELOPE code are presented and used to determine lateral spread and penetration of these beams. It is shown that the penumbra is comparable to photon beams at depths less than 10 cm and the practical range (R_p) of these beams is greater than 40 cm. The depth dose distribution of electron beams compares favourably with photon beams. Effects caused by nuclear reactions are evaluated, including increased dose due to neutron production and induced radioactivity resulting in an increased relative biological effectiveness (RBE) factor of <1.03.

1. Introduction

Megavoltage photon beams are the most widely used radiotherapy modality. Efforts to improve photon beam therapy, i.e. maximize tumour/normal dose ratio (TNR), include three-dimensional treatment planning (3DTP) and dynamic multileaf collimation (DMLC). 3DTP allows visualization of dose distribution from non-coplanar beams. DMLC ideally allows the operator to treat a range of beam orientations with radiation continuously 'on', minimizing the time for a given treatment. DMLC, combined with 3DTP, is perhaps the most promising development for photons to achieve truly three-dimensional intensity modulated radiation therapy (IMRT).

Current modes of dose delivery incorporating IMRT are designed to maximize TNR by effectively maximizing the number of beam portals to be used in as short a treatment time as possible, increasing the total normal tissue volume irradiated and decreasing the maximum dose in that volume. Although the normal tissue complication probability (NTCP) is multifactorially dependent on the volume of tissue irradiated, the maximum dose in that volume and the irradiated organ (Jackson and Kutcher 1993, Kutcher and Burman 1989, Zaider and Amols 1998, Neal *et al* 1995, Lennernas *et al* 1995, Lee *et al* 1994), this paper assumes the principles upon which IMRT is based and proposes a new treatment design based on the same.

The capability of scanning eliminates the need for blocks, multileaf collimators and DMLC, thereby reducing the functional dependence on several moving mechanical parts and increasing the reliability of accurate dose delivery. Additionally, intensity modulation could be achieved more efficiently with a scanned beam by allowing non-coplanar beam arrangements as relative beam angulation is possible with less reliance on mechanical motion (couch, gantry) and allowing the beam to 'dwell' longer in areas where additional dose is required. Therefore, a

scanned beam would be expected to achieve the most superior TNR as the large number of beams could be utilized in a reasonable dose delivery time.

Clinical electron beams range from 5–50 MeV in energy and are not suitable for treatment of deep-seated tumours (>10 cm). There are two reasons for this: (a) electron beams lack the penetrating ability of photon beams and (b) they exhibit large lateral spread (penumbra) particularly at depths of their practical range, R_p. As the electron energy increases, so too does the penetrating ability resulting in an increased R_p. Therefore, if the electron energy is increased above 150 MeV the R_p of the electron exceeds that of a patient body (>40 cm). For these energies, scattering in air is sufficiently constrained so that pencil beam scanning is possible, in contrast to lower-energy electron beams (below 30 MeV) for which scattering in air is prohibitive for pencil beam scanning.

Very high-energy (VHE) photon beams could also be used separately or in combination with VHE electron beams. Photon beams of maximal energies in the range of 150 MV to 250 MV have characteristics of depth dose deposition similar to reversed VHE electron beams. While VHE electron beams have relatively constant dose values between entrance and a depth of $d_{\max}$ and then decrease to low values close to their exit, VHE photon beams in contrast first increase slowly from low values of dose close to the beam entrance to a maximum value of dose at a depth of $d_{\max}$ and then are relatively flat between $d_{\max}$ and the beam exit. We may notice also, that variation of beam energy may be applied for these beams to regulate the value of $d_{\max}$ in each case so it can coincide with the depth of target volume. VHE photon beams can potentially also be used for sharpening of the penumbra at larger depth.

Intuitive predictions about VHE electron beams cannot be directly verified by measurement as beams of this type are not yet available. Therefore, Monte Carlo simulations provide the most efficient method of verifying beam characteristics and resulting dose distributions. Simple (single, parallel opposed, orthogonal) beam arrangements on homogeneous geometries are evaluated in this paper. Neutron production and estimated dose contributions from both neutrons and induced radioactivity are also evaluated.

2. Methods and materials

2.1. Computation with PENELOPE

The data on spatial dose distribution from high-energy electron beams have been computed by the general-purpose Monte Carlo code PENELOPE (Baro *et al* 1995). PENELOPE is a Fortran-77 subroutine package which simulates electron, positron and photon transport. This program realizes the mixed simulation algorithm of PENELOPE (PENetration and Energy LOss of Positrons and Electrons) which was designed initially to simulate electron and positron transport in the energy range from 100 eV to 1 GeV (Baro *et al* 1995) and later photons (Sempau *et al* 1997, Salvat *et al* 1996).

PENELOPE's subroutines are called on from the main program written by the user which steers the geometry and scoring. A spatial grid is considered which comprises elementary scoring spatial bins called voxels. The dose value in a given j-voxel is calculated as

$$D_j = \frac{1}{NV} \sum_{i=1}^{N} \sum_{k=1}^{M} \xi_{k,i,j} \tag{2.1}$$

$$\xi_{k,i,j} = \begin{cases} DE_{k,i} & \text{if } \vec{r} \in \text{voxel}_j \\ 0 & \text{if } r \notin \text{voxel}_j \end{cases} \tag{2.2}$$

where N is the number of simulated particles, $\xi_{k,i,j}$ is the contribution to energy deposition in

a given voxel j by the event k on a given trajectory i, M is the number of inelastic events at the trajectory i, V is the volume of a voxel, $DE_{k,j}$ is the energy loss that takes into account the generation of secondary particles in an inelastic event k at the trajectory j and $\vec{r}$ is the radius-vector of an electron.

The cut-off parameters, i.e. the energy cut-off for the primary electron trajectory tracing EABS(1), photon tracing EABS(2), positron tracing EABS(3), the cut-off energy WCC for hard inelastic collisions, the cut-off energy WCR for hard bremsstrahlung emission, are prescribed to be equal in simulation. The values of the cut-off energy were chosen such that the continuous slowing down approximation (CSDA) range associated with the residual electron energy was sufficiently less than the characteristic size of the voxel.

The mixed algorithm is controlled inside PENELOPE by the use of two parameters prescribed in an input file: C_1, which determines the average angular deflection, and C_2, which is the maximum average fractional energy loss between consecutive hard elastic events. Tests of transmission coefficients and average transmission energy for various combinations of C_1 and C_2 shows stability of studied values relative to variation of the simulation parameters. C_1 has been chosen to be 0.1 and C_2 to be 0.09 for all simulations. These values have been chosen for optimal performance of the simulation algorithm.

PENELOPE's results are compared with experiment and with the ITS code for a single beam measurement. The experiment was performed in a solid water phantom using Gafchromic (ISP technologies Inc.) film on ORELA (the Oak Ridge electron linear accelerator) for an approximately 150 MeV beam of 2 cm radius. PENELOPE calculations are compared with experimental data averaged over a 0.4 cm width on the central axis of the beam (figure 1(*a*)). The ORELA beam, designed for neutron production in research, lacks the stability at comparatively low electron fluences needed for clinical measurement. Taking into account the fact that experimental data have been collected for a beam not ideally monoenergetic (at 150 MeV) and some contamination of the experimental beam by scattered electrons was present, results are in good agreement. Beams from a racetrack microtron can be expected to exhibit superior stability of beam energy and more control over electron fluence. Results for PENELOPE are in agreement with ITS calculations (figure 1(*b*)) (Andreo *et al* 1992).

2.2. Resolution of scanning beam

One of the important questions in electron scanning beam therapy is the determination of the pencil beam size at the patient surface. The pencil beam size determines to a large extent the resolution of the intensity modulation on the surface and thus strongly influences the dose distribution shaping capability of the scanning beam at the depth of treatment. These investigations are necessary as one may expect that quite negligible angular spread of electrons in air may lead to non-negligible spatial widening of the VHE electron beam due to relatively large distances that the beam passes. The scattering of monoenergetic electron beams in air for a few different initial beam energies is investigated.

2.3. Spatial dose distribution in a phantom

Spatial dose distributions in a homogenous phantom for a single VHE electron beam, parallel opposed VHE electron beams and perpendicular VHE electron beams of energies 150 MeV, 200 MeV and 250 MeV are simulated in a 30 cm $\times$ 30 cm $\times$ 30 cm water phantom. All particles are monoenergetic and set in motion perpendicular to the surface of the phantom. Uniformly distributed particles constitute beams of 1 cm radius and 5 cm radius. Dose deposition is scored in the phantom and compared with 15 MV clinical accelerator x-ray beams (energy

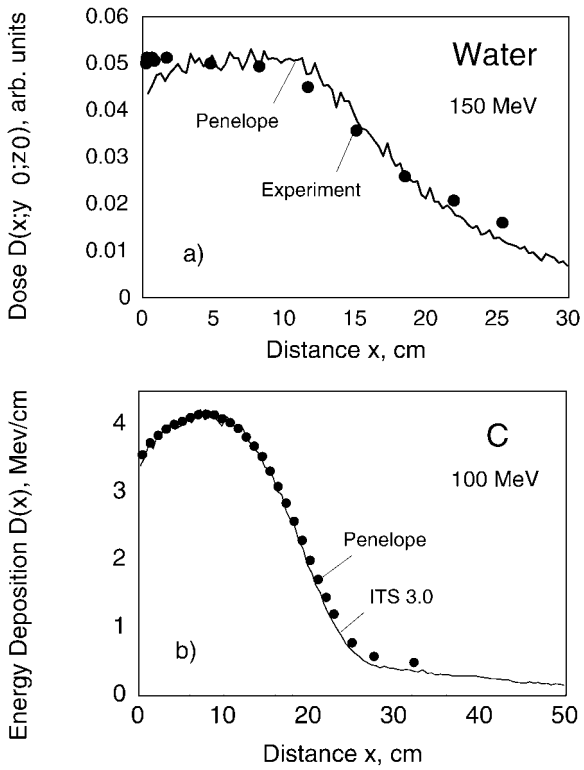

Figure 1. (*a*) Experimental data (points) from ORELA measurements compared with the simulation results (curve) of PENELOPE for 150 MeV electron beam in water phantom and (*b*) comparison of PENELOPE results (points) with the ITS 3.0 results (curve).

spectrum based on Mohan and Chui (1985)). Dose distributions for 15 MV clinical accelerator x-ray beams are obtained by simulation of photon beams that are geometrically identical to simulated VHE electron beam treatments.

Dose distribution in a partial spherical phantom from electron beams of energies 150 MeV and 200 MeV was compared with 15 MV photons. The phantom was simulated with parallel opposed beams, the outline of which were tangential to the surface of the volume S_{cut}. S_{cut} has been assumed to be a portion of the sphere with radius 15 cm cut out from the rest of the sphere by plane that crossed the sphere at the distance of 5 cm from its centre (see figure 2). Parallel opposed VHE electron beams irradiate the S_{cut} domain uniformly with initial particles all set in the same direction (parallel to the base of S_{cut}). Initial particles were set uniformly over the cross section of the beam.

2.4. Evaluation of neutron production

Clinical application of very high-energy electron beams requires careful consideration of dose contribution to the patient from neutrons and from induced radioactivity. The quantitative evaluation of neutron and radioactivity production is also important from the standpoint of radiation protection. In this paper these evaluations are based primarily on data previously published in the literature (Barbier 1969, Swanson 1978, Nedoresov and Ranuk 1989, Code of Federal Regulations 1991).

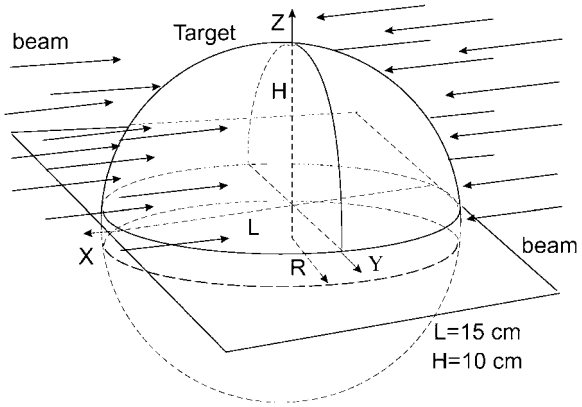

Figure 2. Geometry of the phantom and configuration of beams used in simulation of the irradiation of a partial phantom sphere by parallel opposed VHE electron beams. The length, L, at the base plane is 15 cm and the height, H, from the centre of the base plane to the surface is 10 cm.

The mechanism of neutron production in the region of electron beam energies under consideration is determined by photodivision of nuclei by bremsstrahlung photons and the small contribution of electrodivision by electrons. The main channels of neutron production in a target for these energies are (γ, n), (γ, p), $(\gamma, 2n)$ and (γ, pn) reactions. Considering the bremsstrahlung spectrum we can select two regions of photon energy with respect to mechanisms of neutron production. The first is the region of a giant dipole resonance phenomenon ($E \lesssim 50$ MeV) and second one is the region of energies above the giant resonance. The detailed review of experimental results on photo-nuclear reactions in the giant resonance region and above has been presented by Nedoresov and Ranuk (1989); the data on the cross section of photo-nuclear reactions can be taken from the EXFOR data base EXFOR (IAEA 1985).

The giant dipole resonance phenomenon occurs at photon energies of 25 MeV for light nuclei 14 MeV for heavy nuclei (Barbier 1969). The field of giant dipole resonance begins above the threshold of the (γ, n) reaction, which is approximately equal to the binding energy of a nucleon. A photon wavelength whose energy is less than 30 MeV exceeds the size of nucleus; thus the photon interacts with the 'nucleus as a whole'. Since the cross section for photoabsorption in this region has a resonance form, the cross section of one of the main channels of nuclear de-excitation, i.e. decay with the production of a neutron, has a resonance form too. The main mechanism of neutron production in this region of energy is the evaporation of neutrons from the excited nucleus. Therefore, the angular distribution of neutrons in giant resonance is isotropic, and energy spectrum is of the Maxwell type

$$N(E_n) \simeq E_n \exp\left(-\frac{E_n}{T}\right) \tag{2.3}$$

where $N(E_n)$ is the number of neutrons with energy E_n, T is the nucleus temperature, which is as a rule of the order of 1–2 MeV.

Above the giant resonance, the nuclei–nuclei shower is initiated in the nucleus prior to evaporation of neutrons by interactions of photons with the nuclear clusters. This channel of neutron production is important for high-atomic-number materials. During the shower, parts of nuclei reach energies which exceed the nuclear potential and are expelled. The probability of reactions involving the photoproduction of π mesons is about 1000 times less than that for giant resonance reactions and will not be considered further.

The yield of neutrons increases as the upper limit of the bremsstrahlung spectrum increases. From experimental data, the neutron spectrum in this region reaches a maximum in the low-energy region and rapidly decreases with neutron energy. The average energy of the neutrons produced is of the order of a few MeV, in agreement with the evaporation model. The angular distribution of neutrons is close to isotropic in materials of interest for radiation therapy applications.

The yield of neutrons can be evaluated in a theory of cascade processes according to Swanson (1978) as

$$Y = 0.572 \frac{E_0 X_0 N_0}{A} \int_{E_{\text{th}}}^{E_0} \frac{\sigma(E_\gamma)\,\mathrm{d}E_\gamma}{E_\gamma^2} \tag{2.4}$$

where Y is the yield or interactions per incident electron, E_0 is the incident electron energy, X_0 is the radiation length, (in water X_0 equals 37.1 g cm^{-2}), N_0 is Avogadro's number, A is the atomic number of the material and $\sigma(E_\gamma)$ is the cross section for a photonuclear reaction as the photon energy lies between E_γ and $E_\gamma + \mathrm{d}E_\gamma$; and finally E_{th} is the threshold of the hadron's photoabsorption.

The evaluation of the integral is given in the form

$$\int_{E_{\text{th}}}^{E_0} \frac{\sigma(E_\gamma)\,\mathrm{d}E_\gamma}{E_\gamma^2} = \frac{A^{\frac{5}{3}}}{444} \text{ mbarn MeV}^{-1}. \tag{2.5}$$

Other photo-nuclear reactions in the energy region under consideration are (γ, p), $(\gamma, 2n)$ and (γ, pn). The (γ, p) reaction is responsible for yielding approximately half of the neutron reactions and induced radioactivity produces isotopes of much shorter half-lives. All other reactions are at least an order of magnitude smaller than the (γ, n) reaction. To be conservative from a radiation protection standpoint, the photonuclear reaction yield from giant resonance was assumed to be producing neutrons only.

The number of particles needed to produce 1 cGy in 1 cm^3 of tissue for electrons is approximately of the order of 10^7 particles per cm^2, for neutrons, most conservatively estimated; this value is 10^8 particles per cm^2 at the point of the dose maximum (Barbier 1969). This evaluation is close to that given in by the Code of Federal Regulations (1991).

3. Results and discussion

3.1. Monte Carlo simulations

A set of Monte Carlo simulations in a homogeneous medium (water) is performed for the purpose of evaluating the dose distributions from VHE electron beams. Results of these simulations are presented below. Two million particles are used for the initial simulations with voxel size 0.3 cm for 1 cm radius and 0.5 cm for 5 cm radius. The evaluated statistical uncertainty is less than 3% for a beam of radius 1 cm and 11% for a beam of 5 cm radius.

3.2. Homogeneous cuboid phantom

3.2.1. Single beam dose distribution.

Beam properties at the surface. The passage of the beam through air is simulated by PENELOPE. The intensity (planar fluence) $I(x, r)$ of the pencil beam is scored at plane P_x perpendicular to the beam axis, and situated at a distance x from the vacuum window, and at a distance r from the axis of the beam (symmetry of planar fluence relative to rotations around beam axis is assumed). Let $\Delta_{(0.9,0.1)}(x)$ be defined on P_x as equal to the separation

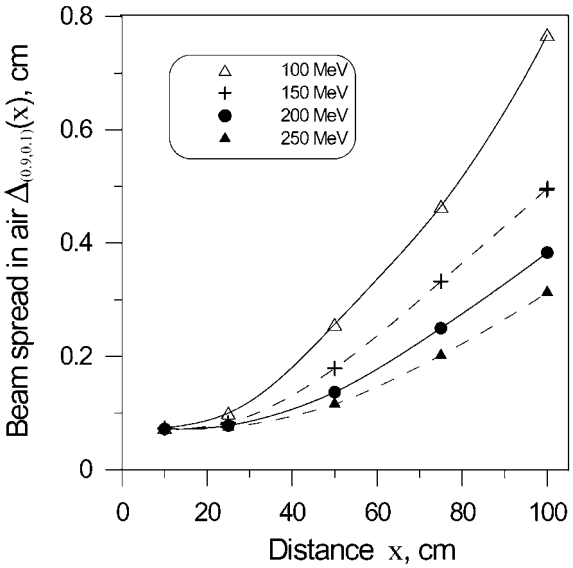

Figure 3. The spread $\Delta_{(0.9,0.1)}(x)$ in air of the electron beam with Gaussian intensity distribution (FWHM = 0.86 mm) versus distance x from the vacuum window of an accelerator for various initial electron energies. $\Delta_{(0.9,0.1)}(x)$ is calculated as the separation between points where intensity, I, decreases from $I = 0.9$ to $I = 0.1$ relative to the maximum value $I(x, 0)$ at a given distance x.

distance between points where the intensity of the beam decreases from $I = 0.9$ to $I = 0.1$ relative to the maximum value $I(x, 0)$ of the beam on P_x.

Figure 3 shows the results of calculations of $\Delta_{(0.9,0.1)}(x)$ for various initial beam energies. For these calculations the distribution of the intensity of particles in the plane at the level of the vacuum window has been assumed to be a two-dimensional, rotationally invariant Gaussian with half width d (half the maximum value at $r = 0$) equal to 0.86 mm with an angular spread of particles at each point of this plane being also a two-dimensional, rotationally invariant Gaussian with half width α equal to 0.43 mrad (Joreskog, private communication). It can be seen from this figure that the spread of the beam at a distance of 50 cm is slightly less than half the spread at a distance of 100 cm and that the value of this ratio is almost independent of beam energy. This rather strong dependence of beam spread on the distance from the vacuum window to the surface suggests that this distance should be kept as small as possible for the sake of high resolution in scanning beam intensity modulation. For beams below 200 MeV this distance should not be not greater than 70 cm.

Depth dose characteristics. A set of two-dimensional dose distributions from single VHE electron beams is displayed in figures 4–5 where isodose curves and isodose surfaces of planar sections of cylindrical beams of energies 150 MeV, 200 MeV and 250 MeV are presented for beams of radius 1 cm and 5 cm. The centre of the coordinate system is placed at the centre of the phantom. It is seen from these figures that VHE electron beams have a relatively small spread in a water up to depth of 10 cm. Moreover, a considerable number of particles penetrate through a 30 cm thick phantom in all cases presented.

One of the most important characteristics is the large depth of dose maximum, $d_{\max}$. There is a strong dependence for VHE electron beams of $d_{\max}$ and the steepness of the dose gradient beyond $d_{\max}$ on the geometrical size of the beam, not unlike the case for low-energy electron beams. For comparison the analogous data for dose distributions from 15 MV accelerator

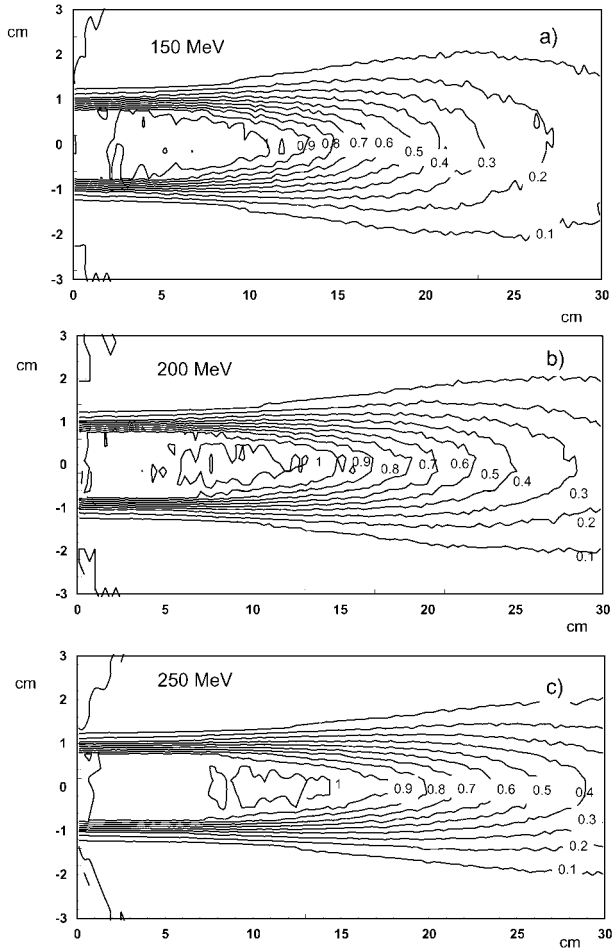

Figure 4. (*a*)–(*c*) Display of isodose curves and (*d*)–(*f*) display of dose surfaces for the central axis beam plane for a single 1 cm radius electron beams of 150, 200 and 250 MeV respectively. Beam axes are perpendicular to the phantom surface.

x-ray beams is presented in figure 6. The most compelling difference between VHE electron and x-ray beams is the deep penetration of high dose values for VHE electron beams. One can expect this property of VHE electron beams to lead to the enhancement of TNR in multibeam treatments. Except for very shallow tumours, the maximum dose delivered to the normal tissue will always be greater for photon beams than for VHE electron beams; what may be of concern is the dose delivered to the total volume, i.e. the integral dose. To illustrate this, table 1 presents comparisons of total energy deposited inside and outside the beam channel, as a ratio to total energy deposited in phantom for 15 MV photon beams and high-energy electron beams. Beam channel here means the cylindrical region in a phantom with radius equal to the beam radius and whose axis is the same as the beam axis. It is seen from these data that the distribution of energy inside and outside the beam channel for a high-energy electron beam is comparable with that for a 15 MV accelerator x-ray beam.

Results of penumbra for single beams are presented in table 2. Penumbra is measured as the distance between the 90% and 20% intensity levels normalized to the maximum value

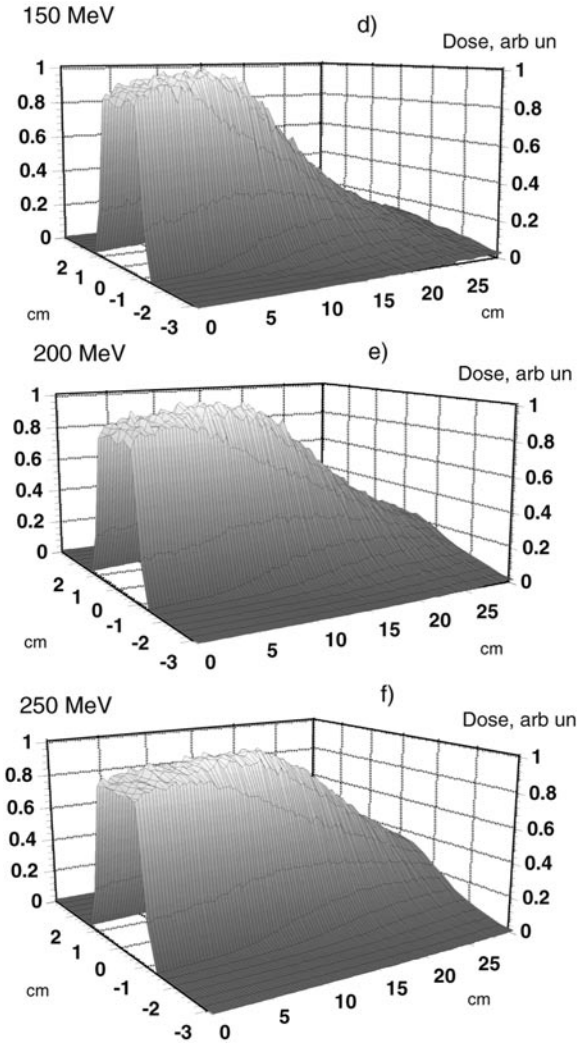

Figure 4. (Continued)

Table 1. Total energy deposited by a single beam inside and outside the beam channel as a ratio to total energy deposited in a phantom.

Energy (MeV)	Mode	Dose in beam channel	Dose outside beam channel
100	Electron beam	0.35	0.65
150	Electron beam	0.41	0.59
200	Electron beam	0.45	0.55
250	Electron beam	0.48	0.52
15	Photon beam	0.49	0.51

at a given depth. For depths $\leqslant$5 cm, the penumbra for VHE electron beams is the same as, or better than, for photon beams. For depths 10–15 cm, VHE electron beams penumbra (as defined above) exceed 15 MV photon penumbra by 1.6 mm to 6 mm depending on depth and energy.

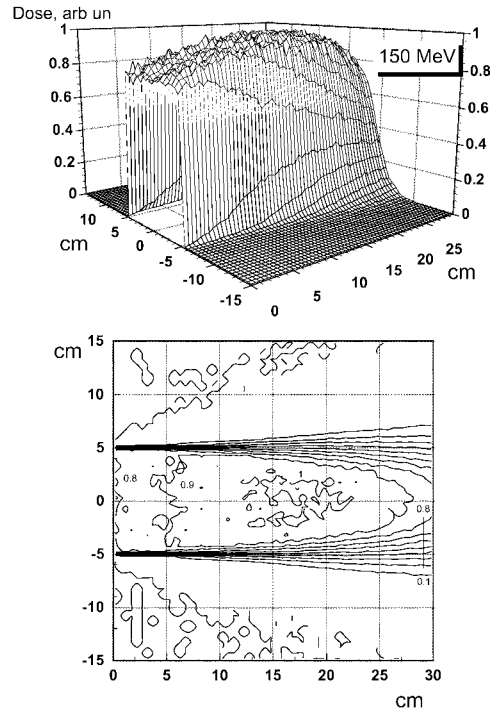

(*a*)

Figure 5. (*a*), (*b*) Display of dose surfaces and isodose curves for the central axis beam plane for single 5 cm radius electron beams of 150 and 200 MeV, respectively. Beam axes are perpendicular to the phantom surface.

Table 2. Penumbra (measured as the distance between 90% and 20% of dose maximum at a given depth) for single electron and photon beams.

	Penumbra (cm)				
Depth (cm)	150 MeV	200 MeV	250 MeV	15 MV	6 MV
1	0.37	0.37	0.34	0.39	0.39
5	0.41	0.41	0.37	0.44	0.45
10	0.79	0.69	0.61	0.44	0.45
15	1.10	0.95	0.83	0.45	0.45

3.2.2. Parallel opposed beams. The simplest combination of beams is the arrangement where two parallel opposed beams are set against each other on opposite sides of the phantom (body). For photon beams this arrangement is applied as it is desirable that the maximum dose outside the target will not be too high relative to the maximum dose inside the target. For VHE electron beams, centrally located targets of typical size (>4 cm) can receive maximum dose in the irradiated volume, thereby resulting in an increased TNR over photon beams.

Figure 7 presents results of simulations for parallel opposed VHE electron beams of energies 150 MeV, 200 MeV and 250 MeV for beams with 1 cm radius, and figure 8 presents 200 MeV beams of 5 cm radius. Results for parallel opposed accelerator beams of energy 15 MV are given for comparison in figure 9. For VHE electron beams, a well defined dose maximum is achieved at the midplane between the opposite surfaces of the phantom; dose

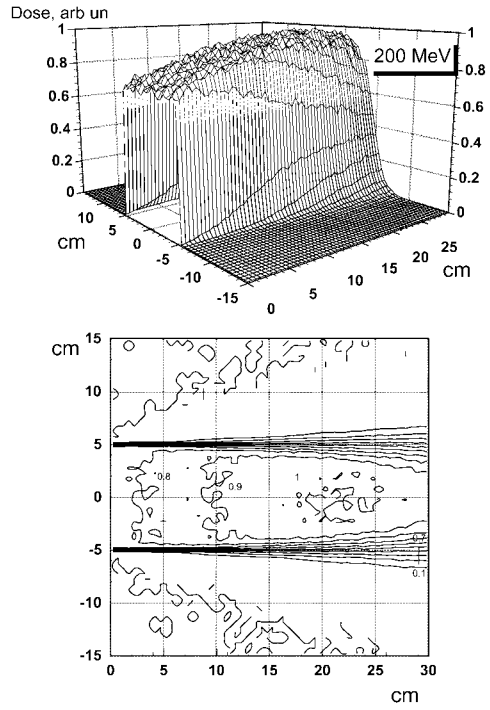

(*b*)

Figure 5. (Continued)

distributions for photon irradiation reach a maximum value close to the surface. It should be also noted that the sharpness of the peak of dose distribution varies with the energy of the electrons.

For parallel opposed VHE electron beams and 15 MV photon beams, the following parameters are compared quantitatively (a) penumbras at different depths for these beams (table 3) and (b) the ratio of the integral doses inside the central region (mid-phantom) of the beam channel to the integral dose of the whole beam channel (table 4). The length, L, in this table refers to the length of the central region along the central axis. In other words, for $L = 2$ cm in a 30 cm phantom, the central region extends from 14 cm depth to 16 cm depth. The integral dose (energy) deposited in this region is then compared with the integral dose (energy) deposited in the beam channel between entrance to exit surfaces. These values characterize the integral tumour to integral beam channel dose ratio for centrally located tumours of various sizes. These values are generally higher for parallel opposed VHE electron beams than for 15 MV photon beams. This ratio varies with phantom thickness and the beam energy and can be optimized by appropriate matching of these parameters.

The penumbra is measured as the distance between the 90% and 20% intensity levels normalized to the maximum at a given depth. One may conclude from these results that penumbras for VHE electron beams and medical accelerator photon beams are comparable. For small depths (less than 5 cm) VHE electron beams have a narrower beam penumbra than photon beams while for larger depths (10 cm to 15 cm) VHE electron beams have a wider beam penumbra than photon beams. In neither case is the difference in the width of the penumbra large enough to indicate a meaningful clinical advantage to VHE electron beams or photon beams.

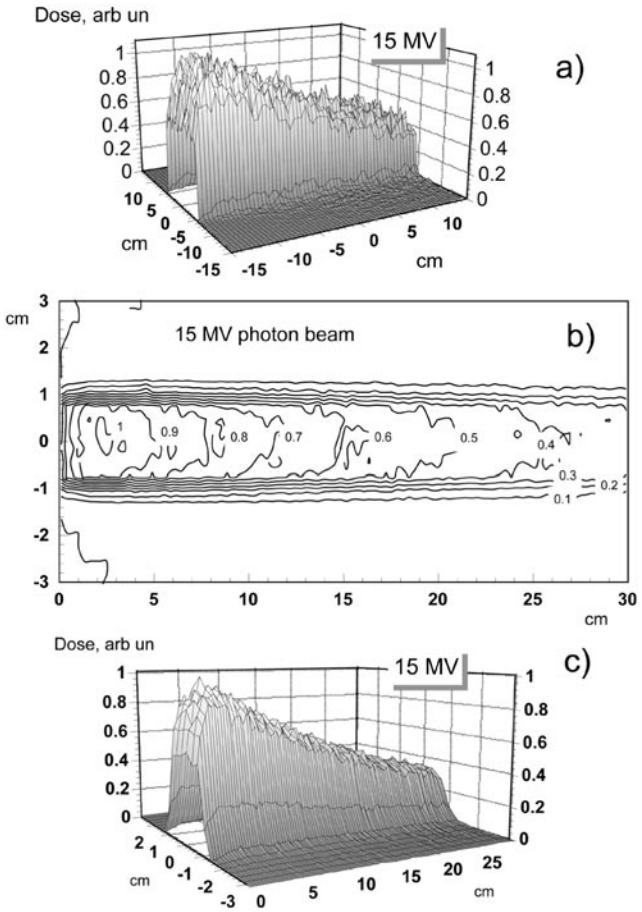

Figure 6. (*a*) Display of dose surface for the central axis beam plane for a single 5 cm radius 15 MV photon beam. (*b*), (*c*) Display of isodose curves and dose surface for the central axis beam plane for a single 1 cm radius 15 MV photon beam. The beam axis is perpendicular to the phantom surface and the centre of coordinates is placed in the middle point of the phantom.

Table 3. Penumbra (measured as the distance between 90% and 20% of dose maximum at a given depth) for parallel opposed electron and photon beams.

	Penumbra (cm)			
Depth (cm)	150 MeV	200 MeV	250 MeV	15 MV
1	0.45	0.54	0.55	0.41
5	0.52	0.59	0.61	0.55
10	1.02	0.83	0.79	0.60
15	1.08	0.95	0.81	0.60

3.2.3. Dose distributions at intersection of perpendicular beams. Figures 10 and 11 present results of simulations for intersecting, perpendicular 1 cm radius 200 MeV VHE electron beams and 15 MV photon beams. For beams that intersect at relatively large depth (15 cm), dose distributions at the intersection of two perpendicular VHE electron beams have almost

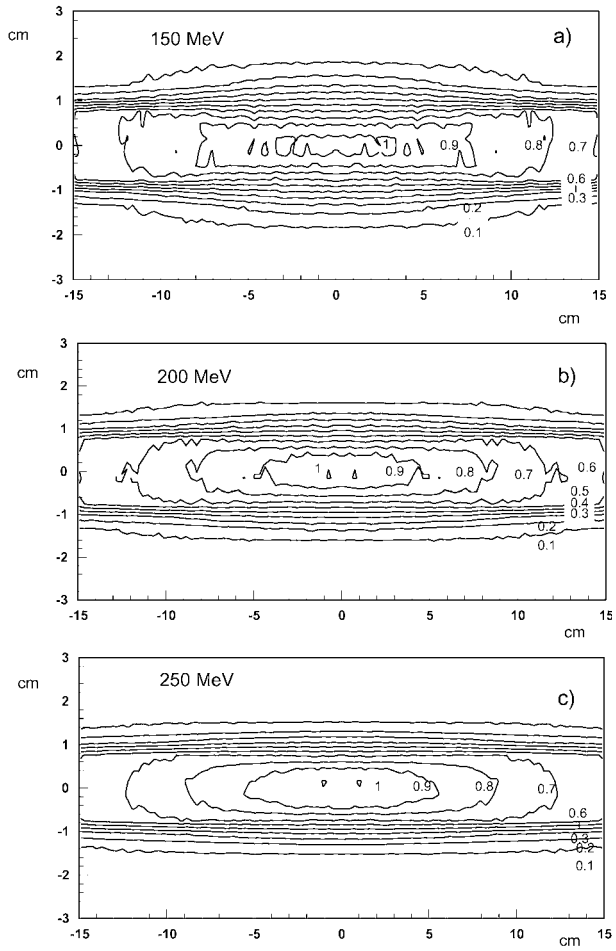

Figure 7. (*a*)–(*c*) Display of isodose curves, (*d*)–(*f*) display of dose surfaces for the central axis beam plane for parallel opposed 1 cm radius electron beams of 150, 200 and 250 MeV respectively. Beam axes are perpendicular to the phantom surface and the centre of coordinates is placed in the middle point of the phantom.

Table 4. Total energy deposited in a section of the beam channel (cylinder with beam radius of 2 cm and length L) as the ratio to the total energy deposited in the beam channel.

L (cm)	15 MV photons	150 MeV electrons	250 MeV electrons
2	0.08	0.09	0.097
4	0.16	0.176	0.181
8	0.28	0.306	0.314
10	0.36	0.390	0.402

rotational symmetry and characteristic increase in dose towards the centre of the intersection of the volume.

For 5 cm radius standard radiotherapy applications (see figure 12) the most important characteristics of dose distribution at the intersection of perpendicular VHE electron beams is the more uniform dose distribution throughout the volume of intersection (no wedging

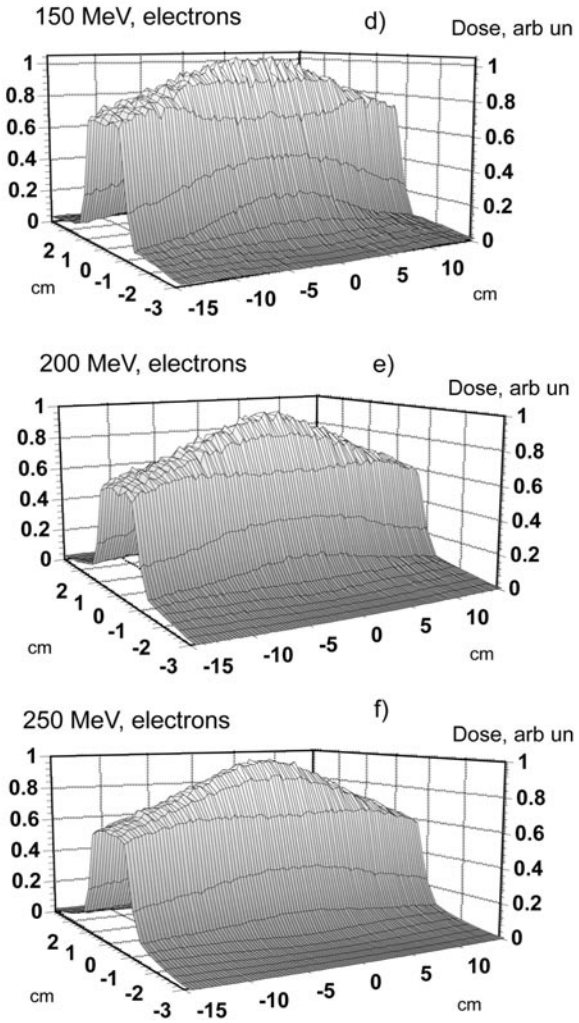

Figure 7. (Continued)

Table 5. The surface dose for parallel opposed 150–200 MeV electron beams and 10 MeV photon beams. Data are given as percentage of the maximum of spatial dose distribution in phantom.

Energy (MeV)	Mode	Surface dose
15	Photons	45%
150	Electrons	70%
200	Electrons	60%
250	Electrons	60%

effect). This uniformity of dose distribution results from increased depth dose uniformity throughout the beam channel for VHE electron beams in comparison to clinical photon beams. Therefore, shaping beam profiles with wedges, while necessary for photon beams to achieve uniform dose for perpendicular beam arrangement, is not necessary for VHE electron beams.

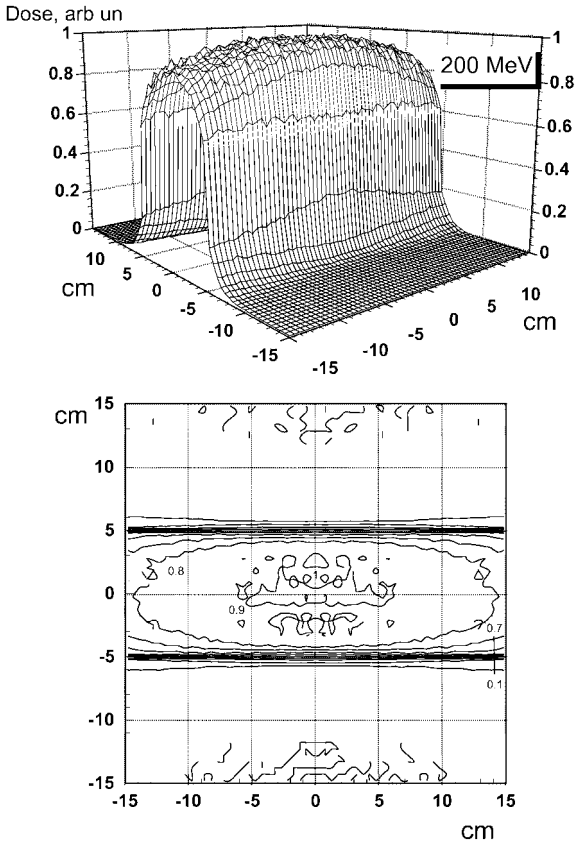

Figure 8. Display of dose surface and isodose curves for the central axis beam plane for parallel opposed 5 cm radius electron beams of 200 MeV. Beam axes are perpendicular to the phantom surface and the centre of coordinates is placed in the middle point of the phantom.

3.3. Consideration of surface dose for single, parallel opposed and orthogonal beams

Results for surface dose are given in table 5.

Surface dose may be a limiting factor in some applications of VHE electron beams in radiation therapy. This is in contrast to photon beams that offer significant skin sparing in all circumstances. When contributions from scattered photons and secondary electrons are minimized the surface dose for megavoltage x-ray beams from modern accelerators can be as low as or lower than 20% of the dose at $d_{\max}$. On the other hand, the surface dose for VHE electron beam can be as high as 90–95% of the dose at $d_{\max}$. For treatments with multiple beams, the relative surface dose decreases. For example, with parallel opposed beams the ratio of surface dose to dose at $d_{\max}$ more than doubles for x-ray therapy while it decreases for VHE electron beams to 60–80% (depending on energy). Thus parallel opposed VHE electron beams are comparable, as far as skin sparing capability is concerned, to photon beams. For two perpendicular VHE electron beams the ratio of surface dose to maximum dose at the intersection of beams decreases to less than 50%, and for the same reason, the ratio of surface dose to maximum dose at intersection of four beams intersecting at the target that do not overlap on the surface of the body decreases to less than 30%. Thus, for multiple VHE electron beam treatments the high skin dose of a single beam is not of clinical concern.

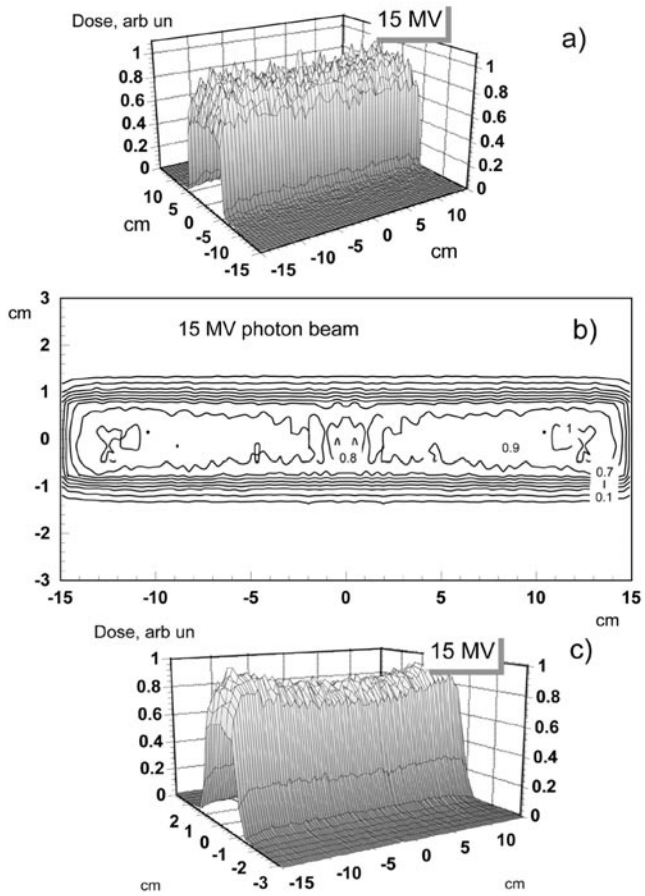

Figure 9. (*a*) Display of dose the surface for the central axis beam plane for parallel opposed 5 cm radius 15 MV photon beams and (*b*), (*c*) display of isodose curves and the dose surface for the central axis beam plane for parallel opposed 1 cm radius 15 MV photon beams. Beam axes are perpendicular to the phantom surface and the centre of coordinates is placed in the middle point of the phantom.

3.4. Spherical phantom

To test the intuitive prediction that compensation due to thickness variation is not required with VHE electron beams, simulations have been performed on a spherical phantom.

Dose distributions in planes intersecting S_{cut} at various elevations over the base plane of S_{cut} and parallel to this base plane are presented in figure 13. The moving window least squares polynomial fit technique (Tabata 1997) was applied to improve the statistical uncertainty of data. This technique is very useful for the particular geometry under consideration, as rather large uncertainties for these simulations can be expected even for millions of histories being simulated (Das 1999).

Results of simulations for VHE electron beams in volume S_{cut} confirm predictions. Due to the fact that there is not much dependence on depth dose inside the beam channel there is little variation in dose in any of the planes cutting volume S_{cut}. Close to the top of the volume S_{cut}, figure 13(*c*), where the phantom is the thinnest, the doses are still no higher than at the plane close to the base of volume S_{cut}, figure 13(*a*), where the phantom is the thickest. These

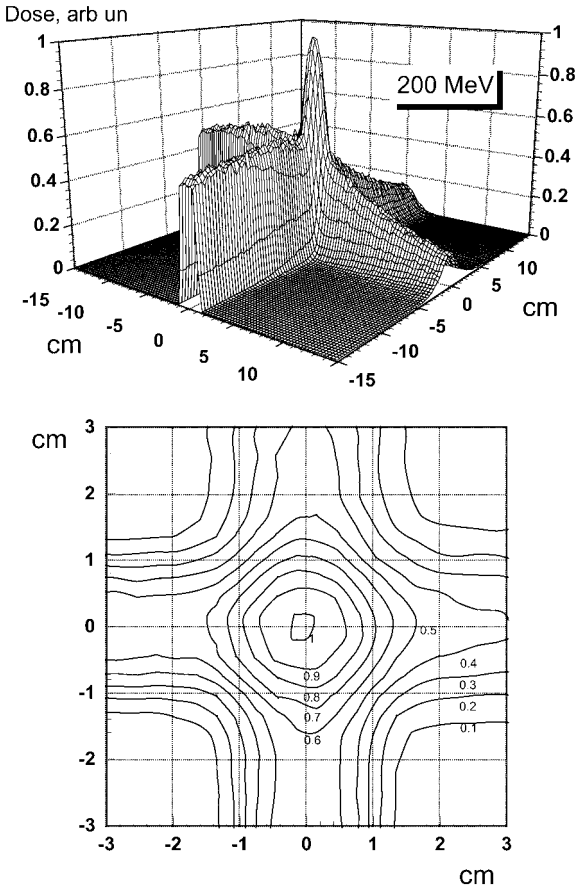

Figure 10. Display of the dose surface and isodose curves for a plane defined by the central axes of two perpendicularly intersecting 1 cm radius, 200 MeV electron beams.

properties of dose distributions from VHE electron beams clearly contrast with properties of dose distributions in volume S_{cut} from photon beams (e.g. breast treatment). They also clearly indicate that VHE electron beams would not require as much modulation of beam intensities as photon beams. In particular, there is no need for these beams to compensate for the non-uniformities caused by the unequal contour at the surface as thickness variation does not lead to non-uniform dose distributions in the irradiated volumes.

3.5. Evaluation of bremsstrahlung and neutron production

VHE electron beams lose a large part of their initial energy to bremsstrahlung production. The data on bremsstrahlung production is important from a radiation protection standpoint and will dictate the amount of shielding required.

Typical bremsstrahlung spectra and angular distributions in a thick water phantom for various initial energies are illustrated in figures 14 and 15. It is seen from these figures that the number of photons increases to a maximum on the low-energy end of the spectrum (which is not shown due to scaling on the graph). The angular distribution of bremsstrahlung photons is sharp. Thus the main contribution to dose distribution due to bremsstrahlung will be along the channel of the initial electron beam.

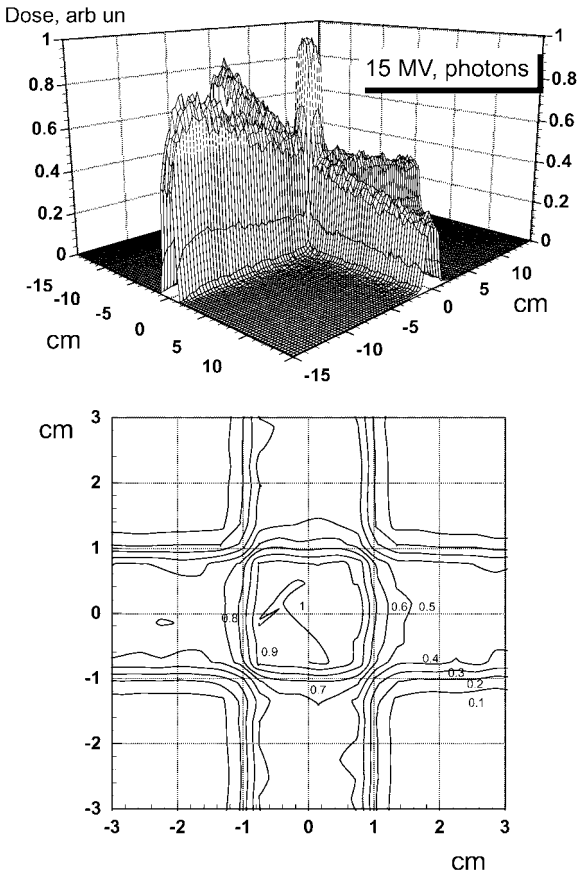

Figure 11. Display of the dose surface and isodose curves for a plane defined by the central axes of two perpendicularly intersecting 1 cm radius, 15 MV photon beams.

Using equation (2.4) with substitution (2.5), the neutron yield can be evaluated. The yield of neutrons for electron beams of 150 MeV and 200 MeV is 0.027 and 0.037 neutrons per incident electron respectively. From Barbier (1969) the giant resonance yield per electron per MeV (Y/E_0) is approximately 6×10^{-5}. In order to deliver a typical daily dose of 200 cGy through pencil beam to $d_{\max}$ depth, evaluations based on Barbier (1969) result in the number of particles in the beam being equal to 2×10^9. Based on this number of incident particles, we can evaluate the neutron flux utilizing techniques described in section 2.4. The neutron flux is 5.5×10^7 and 7.3×10^7 neutrons per cm^2 for electron beams of 150 MeV and 200 MeV respectively. Using flux-to-dose conversion coefficients given by Barbier (1969) we calculate an approximate 0.2% increase in dose due to fluence of neutrons at the point of maximum dose. The quality factor for neutrons is taken conservatively as 10 (Hall 1994) resulting in an increased RBE factor of 1.02 accounting for dose equivalent from neutrons should be used for dose prescription in VHE electron beam therapy.

Dose equivalent correction may also be expected due to induced radioactivity of oxygen, carbon and nitrogen inside the human body. There is some inverse dependence on mass number for these three elements; however, this dependence leads to a difference in yield of less than one order of magnitude. Therefore for the very simple model that seems to be adequate for our purposes, we will assume equal cross sections for photoneutron production and we will

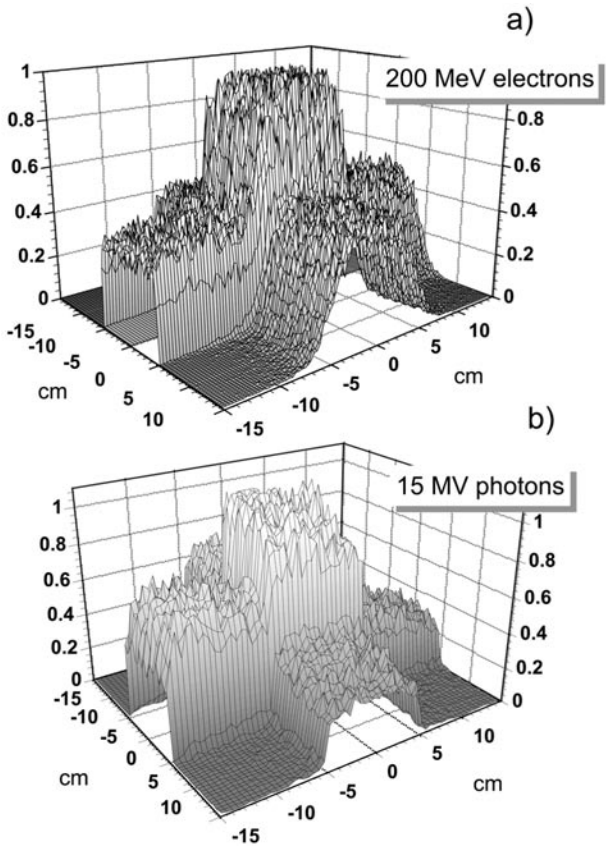

Figure 12. (*a*) Display of the dose surfaces for a plane defined by the central axes of two perpendicularly intersecting 5 cm radius 200 MeV electron beams. (*b*) Display of dose surfaces for the plane defined by the central axes of two perpendicularly intersecting 5 cm radius 15 MV photon beams.

base the number of radioactive atoms on the abundance of each element in tissue. Due to the great simplifications already made for these models, we further make simplified calculations according to Cember (1989), assuming an infinitely large medium containing a uniformly distributed isotope. The increase in dose from induced radioactivity was calculated to be approximately 0.01% of the intended VHE electron beam dose. After accounting for quality factor the dose equivalent factor from induced radioactivity should be only 1.002, and the overall equivalent factor, including neutron and induced radioactivity contribution, should be within 1.02–1.025. This value is rather lower than the previously published dose equivalent factor (1.04–1.05) for relatively high energy beams (up to 50 MeV) of electrons and photons though not quite inconsistent with it (Tilikidis *et al* 1996). Thus we can conclude that neutron and proton production in VHE electron beam therapy should not significantly affect equivalent doses in comparison with photon treatments.

In summary, the induced radioactivity from neutron fluence has been calculated primarily for the (γ, n) reaction in the giant resonance region and above the giant resonance region. The calculated induced radioactivity has been found to be quite small and would be expected to be inconsequential in terms of increased dose. The dose due strictly to the neutron fluence has been found to be more significant and expected to have a greater impact on dose than the

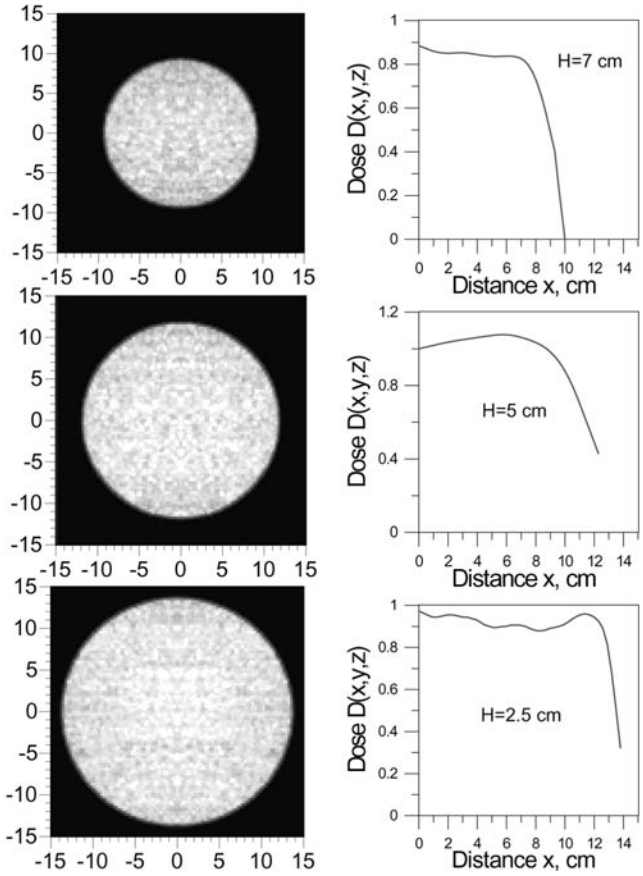

Figure 13. Dose distribution for the beam configuration and geometry described in figure 2 for 200 MeV electron beams at distances of 2.5 cm, 5.0 cm and 7.0 cm from the phantom base.

dose from induced radioactivity but still not significantly different from photons in the range of 30–50 MeV (Tilikidis *et al* 1996). Since the increase in neutron production is approximately linear with increase in energy per electron in the ranges considered here, we can also conclude that the required shielding should not be significantly greater than for 50 MeV electron and photon beams.

4. Summary and conclusion

The results of our simulations of VHE electron beam irradiation of homogeneous media are briefly summarized and possible implications of dose distribution properties for radiation therapy discussed.

4.1. Penetration of large size VHE electron beams

Beams of electrons in the range of energies between 150 and 250 MeV can penetrate far enough into a patient's body that they may deliver a desirable dose distribution to the most deeply situated tumours. Greater penetration is easier to achieve with beams of a larger size.

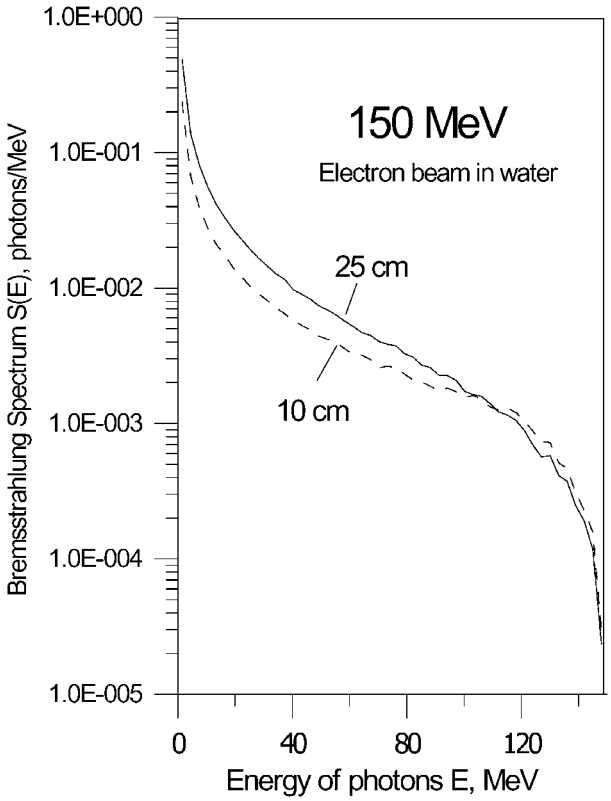

Figure 14. Spectrum of bremsstrahlung photons produced by a 150 MeV monoenergetic electron beam at depths 10 cm and 25 cm in a thick water phantom.

The exit dose for large, single beams of energy 200 MeV for a 30 cm thick phantom is roughly equal to the dose at the entrance, and both dose values are in the range of 80% to 90% of the dose at maximum. Thus using parallel opposed beams of 200 MeV energy should provide an almost uniform dose throughout the beam channel in a phantom as thick as 60 cm. When applying beams of higher energy (i.e. in the range from 200 MeV to 300 MeV) we can even expect a dose increase at the midplane of the 60 cm thick phantom. Matching VHE electron beam energy to separation so that maximum dose is achieved at the tumour depth improves the integral dose ratio (tumour to normal tissue) relative to photon beams.

4.2. Penetration of small size VHE electron beams

Radiosurgery type beams of very high-energy electrons (150 MeV to 200 MeV) achieve completely satisfactory penetration when applied as parallel opposed irradiation for phantoms as thick as 30 cm (40 cm when energy is increased to 300 MeV) with a well defined maximum of dose distribution at the midplane of the phantom. For radiosurgery applications (head) these penetrations completely satisfy the requirements of treatment procedures. Even for a stereotactic body frame (Elekta) of the chest and abdomen (beams as small as 2 cm by 2 cm), penetration of parallel opposed VHE electron beams is completely adequate for treatments.

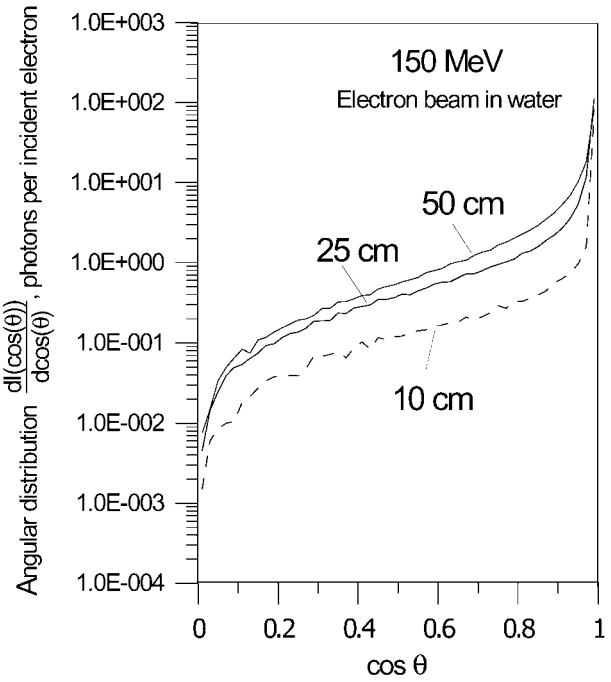

Figure 15. Angular distribution of bremsstrahlung photons produced by a 150 MeV monoenergetic electron beam at depths 10 cm, 25 cm and 50 cm in a thick water phantom.

4.3. Penumbra

Calculations of dose distributions for VHE electron beams that have been presented indicate that for parallel opposed beams the sharpness of the penumbra for VHE electrons is of comparable quality to the sharpness of the penumbra for clinical photon beams. Penumbras of single VHE electron beams increase with increasing depth and are somewhat less wide than penumbras of single clinical photon beams for depths below 5 cm and somewhat wider for depths above 10 cm. Since photon beams have a more rapidly decreasing depth dose, the central axis dose will be less for greater depths for photon than for electron beams. This means that in absolute terms more 'spread' in photon than electron beams occurs than is actually reflected by values of relatively normalized penumbras evaluated in this paper.

4.4. Option of electromagnetic scanning of pencil VHE electron beams and its consequence for intensity modulation

Intensity modulation in radiation therapy (IMRT) can be understood in a narrow sense (IMRTNS) and in a general sense (IMRTGS). IMRTNS assumes that the source position, and thus also the direction of the central axis of the beam (i.e. the line connecting source with isocentre), is fixed. The beam is modulated, changing the intensity (number/area) of particles passing through various points in the plane perpendicular to the fixed axis of the beam. As long as the modulation for each fixed beam (fixed source position) is treated as independent from any another it should still be treated as IMRTNS. IMRTGS parameters are not contained to points of a plane perpendicular to the fixed axis but also extends over all positions of the source. In other words, IMRTGS modulates mutually interdependent

intensities of all rays that can be applied for the treatment of the target rather than only rays that intersect the target from a few fixed positions of the source (Papiez and Ringor 1997, Ringor and Papiez 1998). Thus only IMRTGS that do not impose any *a priori* restrictions on the choice of the treatment parameters can truly lead to the most optimal radiation therapy.

In its most advanced state DMLC is the most efficient technique for photon beams to achieve conformal dose delivery over many beam orientations. IMRTNS is achieved through dynamic motion of individual leaves for a given beam orientation. Without the possibility of a scanning mechanism, the duration of DMLC treatment is dependent on the large number of mechanical motions of individual leaves for many possible positions of gantry and couch. Let us assume generously that, for example, at a given couch angle and gantry position, the duration of DMLC treatment delivery lasts only 10 s. If modulation is to be iterated by every 5 degrees of the gantry rotation (in fixed positions or in dynamical mode) then a 360 degree rotation will require $(360/5) \times 10 = 720$ s for treatment at a single couch angle. For 10 couch angles, the total 'beam-on' time is then 2 h.

There are only two possible solutions to this dilemma. First is to restrict *a priori* the range of degrees of freedom for couch and gantry motions, and the second is to look for new technology capable of delivering IMRTGS based treatments in shorter periods of time (up to 15 min per fraction) that are also economically viable. This is why electromagnetically scanned VHE electron beam pencil beam therapy should be investigated.

First, irradiation with VHE electron beams requires, in general, less modulation of beam intensities than does irradiation with photon beams. The modulation of beam intensities often arises from the need to compensate for undesirable dose variations caused by differences in photon attenuation due to the uneven surface of the irradiated body. As the above-discussed results on dose distributions in spherical phantom demonstrate, there is almost no variation in dose distribution from VHE electron beams that irradiate phantoms with the most uneven surfaces. These properties of VHE electron beams imply that irradiations with VHE electron beams will, in general, require less intensity modulation to achieve a particular standard of dose distribution than photon beams.

Scanning of a pencil beam as a mechanism of modulation of beam intensity provides an extra degree of freedom for positioning of rays of irradiating particles relative to the target and in consequence eliminates the need for couch rotation during IMRTGS. Rotation of the gantry combined with translational motion of the couch can place the source at any point on the surface of the cylinder, the centre of which can be identified with the centre of the target. The beam scanning ability to change the direction of pencil rays at the source so that they may approach on any point in the vicinity of the target from any point of the surface of the cylinder clearly makes the need for couch rotation redundant.

The speed of electromagnetic scanning of a charged particle pencil beam can potentially decrease the time of IMRTGS by at least an order of magnitude (10 times). The complete modulation of intensity through electromagnetic scanning at a given position of the pencil beam can easily be achieved in 1 s. This can be done, under similar assumptions as in the above discussion of DMLC IMRT, at every 5 degree interval of the rotation of the gantry (or at fixed gantry positions every 5 degrees). Thus treatment for one complete rotation of the gantry will last in this case 72 s ((360 degrees/5 degrees) $\times$ 1 s.) Full treatment would require then that the source of the pencil beam will spiral 10 coils (equivalent to 10 positions of the couch in DMLC IMRT) along the helical trajectory as visible from the target being translated forward on the couch. This will be achieved with 10 full rotations of the gantry that gives the estimate of the time for the scanned, VHE electron IMRTGS as being equal to 720 s.

Acknowledgments

The authors wish to gratefully acknowledge John Cameron (IU Cyclotron) and Erik Joreskog (Scanditronix Medical) for their invaluable assistance and significant contribution to this work.

References

Andreo P, Ito R and Tabata T 1992 Tables of charge and energy deposition distributions in elemental materials irradiated by plane parallel electron beams with energies between 0.1 and 100 MeV *RIAST Report* no 1 (Osaka: University of Osaka Prefecture) pp 1–141

Armstrong J G, Burman C, Leibel S, Fontenla D, Kutcher G, Zelefsky M and Fuks Z 1993 Three-dimensional conformal radiation therapy may improve the therapeutic ratio of high dose radiation therapy for lung cancer *Int. J. Radiat. Oncol. Biol. Phys.* **26** 685–9

Barbier M 1969 *Induced Radioactivity* (New York: North-Holland/American Elsevier)

Baro J, Sempau J, Fernandez-Varea J M and Salvat F 1995 PENELOPE: an algorithm for Monte Carlo simulation of the penetration and energy loss of electrons and positrons in matter *Nucl. Instrum. Methods* B **100** pp 31–46

Berger M J 1963 *Methods in Computational Physics* vol 1, ed B Adler, S Fernbach and M Rotenberg (New York: Academic) p 135

Brahme A 1987 Design principles and clinical possibilities with a new generation of radiation therapy equipment. A review *Acta Oncol.* **26** 403–12

Brahme A, Kraepeliaen T and Svensson H 1980 Electron and photon beams from a 50 MeV racetrack microtron *Acta Radiol. Oncol.* **19** 305–19

Cember H 1989 *Introduction to Health Physics* 2nd edn (New York: Pergamon) pp 150–3

Das I, Moskvin V, Tabata T and Verhaegen F 1999 Monte Carlo simulated data for dose perturbation at high Z interfaces irradiated by kilovoltage photon beams *Med. Phys.* **26** 1122

Fernandez-Varea J M 1998 Monte Carlo simulation of the inelastic scattering of electrons and positrons with optical data model *Radiat. Phys. Chem.* **53** 235–45

Hall E 1994 *Radiobiology for the Radiologist* 4th edn (Philadelphia: Lippincott) pp 445–6

IAEA 1985 EXFOR user's guide *IAEA Publication* 0896/01 (Vienna: IAEA)

Jackson A and Kutcher G J 1993 Probability of radiation-induced complications for normal tissues with parallel architecture subject to nonuniform irradiation *Med. Phys.* **20** 613–25

Joreskog E private communication (Scanditronix Medical Corporation)

Karlsson M, Svensson H, Nystrom H and Stenberg J 1998 The 50 MeV racetrack accelerator. A new approach to beam shaping and modulation *Dosimetry in Radiotherapy* vol 2 (Vienna: IAEA) pp 307–20

Karlsson M and Zackrisson B 1997 Exploration of new treatment modalities offered by high energy (up to 50 MeV) electrons and photons *Radiother. Oncology* **43** 303–9

Kutcher G J and Burman C 1989 Calculation of complication probability factors for non-uniform normal tissue irradiation: the effective volume method *Int. J. Radiat. Oncol. Biol. Phys.* **16** 1623–30

Lee M, Wynne C, Webb S, Nahum A E and Dearnaley D 1994 A comparison of proton and megavoltage x-ray treatment planning for prostate cancer *Radiother. Oncol.* **33** 239–53

Lennernas B, Rikner G, Letocha H and Nilsson S 1995 External beam radiotherapy of localized prostatic adenocarcinoma. Evaluation of conformal therapy, field number and target margins *Acta Oncol.* **34** 953–8

Mohan R and Chui C 1985 Energy and angular distributions of photons from medical accelerators *Med. Phys.* **12** 592–7

Neal A J, Oldham M and Dearnaley D P 1995 Comparison of treatment techniques for conformal radiotherapy of the prostate using dose-volume histograms and normal tissue complication probabilities *Radiother. Oncol.* **37** 29–34

Olsen D R, Kambestad B K and Kristoffersen D T 1994 Calculation of radiation induced complication probabilities for brain, liver, and kidney, and the use of a reliability model to estimate critical volume fractions *Brit. J. Radiol.* **67** 1218–25

Papiez L and Ringor M 1997 Implications of a reconstruction formula for rotational therapy in treatment planning optimization *Inverse Problems* **13** 1519–32

Nedoresov V G and Ranuk Yu H 1989 *Photo-division of Nuclei Above Giant Resonance* (Kiev: Naukova Dumka) (in Russian)

Ringor M and Papiez L 1998 Inverse planning and optimization: a comparison of solutions *Radiat. Phys. Chem.* **53** 263–74

Salvat F 1998 Simulation of electron multiple elastic scattering *Radiat. Phys. Chem.* **53** 247–56

Salvat F, Fernandez-Varea J M, Baro J and Sempau J 1996 PENELOPE, an algorithm and computer code for Monte Carlo simulation of electron-photon showers *Informes Tecnicos CIEMAT* no 799 (Madrid: CIEMAT)

Sempau J, Acosta E, Baro J, Fernandez-Varea J M and Salvat F 1997 An algorithm for Monte Carlo simulation of coupled electron–photon transport *Nucl. Instrum. Methods* B **132** 377–90

Swanson W P 1978 Calculation of neutron yields released by electrons incident on selected materials *Health Phys.* **35** 353–67

The Code of Federal Regulations 1991 Title 10 vol 1 part 20 (26 FR 23391, 10 CER 20 1004-C) US Government Printing Office pp 291–300

Tabata T 1997 Smoothing and interpolation by moving window least squares polynomial fits: application for energy charge deposition distributions by electrons *Bull. Osaka Prefecture University Ser. A* **46** 71–8

Tilikidis A, Lind B, Nafstadius P and Brahme A 1996 An estimation of the relative biological effectiveness of 50 MV bremsstrahlung beams by microdosimetric techniques *Phys. Med. Biol.* **41** 55–69

Yu C X 1995 Intensity modulated arc therapy with dynamic multileaf collimation: an alternative to tomotherapy *Phys. Med. Biol.* **40** 1435–49

Zaider M and Amols H I 1998 A little to a lot or a lot to a little: is NTCP always minimized in multiport therapy? *Int. J. Radiat. Oncol. Biol. Phys.* **41** 945–50